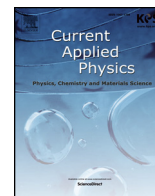




ELSEVIER

Contents lists available at ScienceDirect

Current Applied Physics

journal homepage: www.elsevier.com/locate/cap

Structural properties of ferroelectric heterostructures using coherent bragg rod analysis

Kyeong Jun Lee^a, Yeong Jae Shin^{b,c,d}, Taeyang Choi^a, Tae Won Noh^{b,c}, Hua Zhou^e,
Seo Hyung Chang^{a,*}

^a Department of Physics, Chung-Ang University, Seoul, 156-756, Republic of Korea

^b Center for Correlated Electron Systems, Institute for Basic Science (IBS), Seoul, 08826, Republic of Korea

^c Department of Physics and Astronomy, Seoul National University, Seoul, 08826, Republic of Korea

^d Department of Applied Physics, Yale University, New Haven, CT, 06511, USA

^e X-Ray Science Division, Advanced Photon Source, Argonne National Laboratory, Lemont, IL, 60439, USA

ARTICLE INFO

Keywords:

Ferroelectricity

BaTiO₃SrRuO₃

Coherent bragg rod analysis

X-ray scattering

ABSTRACT

We investigated the crystal structure of SrRuO₃/BaTiO₃/SrRuO₃ (SRO/BTO/SRO) heterostructures grown on a SrTiO₃ (001) substrate using surface X-ray scattering. The interface structure of SRO/BTO/SRO heterostructures can decrease the critical thickness of ferroelectric BTO films reduced to 3.5 unit cells. Owing to weak intensity of ultrathin films, lab-source-based X-ray measurement cannot determine the atomic arrangement of the heterostructures and their lattice parameters. We introduced synchrotron-based X-ray scattering techniques combined with coherent Bragg rod analysis (COBRA) to resolve the details of the heterostructures. We obtained detailed crystal structural information based on the electron density profiles of the SRO/BTO/SRO heterostructures acquired from COBRA results, e.g., lattice parameters and atomic arrangements.

1. Introduction

Oxide heterostructures are proper model systems for exploring emergent physical properties, such as two-dimensional electron gas, metal-insulator transition, superconductivity, and ferroelectricity [1–8]. Recent advances in atomic-level film fabrication can lead to the achievement of physical properties that do not exist in nature [4,9–11]. Numerous researchers have investigated the thickness limit of nanoscale devices for retaining ferroelectricity using ultrathin ferroelectric oxide heterostructures. This limit is referred to as critical thickness [12,13]. The in-depth understanding of the critical thickness of ferroelectric materials provides a basis for miniaturizing nanoscale functional devices and achieving high-density nonvolatile random access memory.

The SrRuO₃/BaTiO₃/SrRuO₃ (SRO/BTO/SRO) heterostructure is a model system for creating oxide heterostructures with atomic control for the critical thickness studies, as shown in Fig. 1. A recent study on this system found that the critical thickness of a ferroelectric BTO film was quite low, i.e., 3.5 unit cells (u.c.) for a BTO layer consisting of three BaO layers and four TiO₂ layers [14]. However, it was extremely sensitive to the interface structure between the ferroelectric BTO layer and SRO electrodes. For instance, a symmetric interface in SRO/BTO/

SRO heterostructures, such as the same SrO–TiO₂ terminations could reduce pinned dipoles and enhance the stability of ferroelectric polarization compared with the different mixed terminations, e.g., RuO₂–BaO and SrO–TiO₂. This preserves ferroelectricity in the ultrathin limit. The main method of elucidating the relation between a structure and ferroelectricity is the direct experimental verification of the atomic arrangement of oxide heterostructures.

Here, we introduce a coherent Bragg rod analysis (COBRA) technique based on surface X-ray scattering, which is a phase-retrieval X-ray diffraction approach [15–21]. It is still difficult to nondestructively determine the structure of ultrathin films with sub-angstrom resolution. For instance, transmission electron microscopy typically requires specific sample treatments and easily perturbs the ferroelectric polarization of samples. Lab-source-based X-ray diffraction cannot be utilized to observe the structure of ultrathin films owing to weak intensity. Synchrotron-based X-ray scattering combined with COBRA can non-destructively obtain an electron density map and a detailed crystal structure through the Fourier transformation of calculated complex structure factors [15,16]. In addition, COBRA can provide a three-dimensional electron density map and reconstruct a crystal structure.

We visualized the atomic-level three-dimensional structure of the SRO/BTO/SRO heterostructures grown on SrTiO₃ (STO)(001) using a

* Corresponding author.

E-mail address: cshyoung@cau.ac.kr (S.H. Chang).

<https://doi.org/10.1016/j.cap.2020.01.015>

Received 13 December 2019; Received in revised form 16 January 2020; Accepted 21 January 2020

Available online 24 January 2020

1567-1739/ © 2020 Korean Physical Society. Published by Elsevier B.V. All rights reserved.

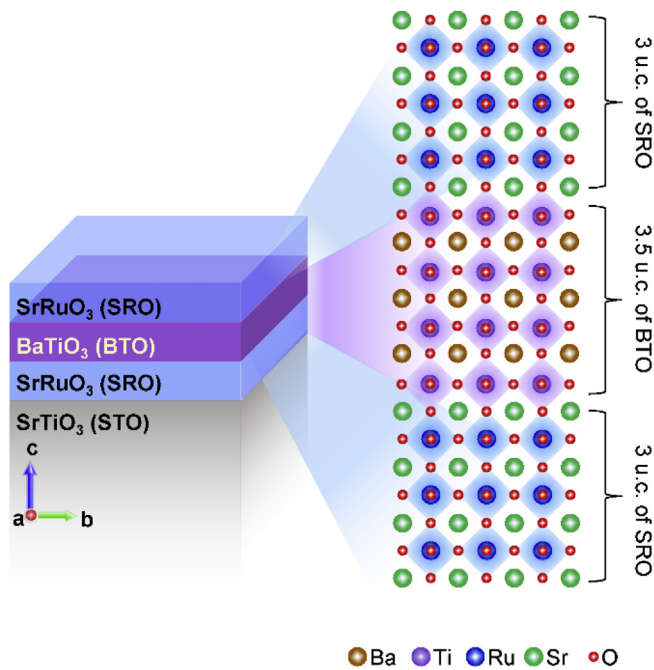


Fig. 1. Schematic of ferroelectric heterostructure model system. The atomic stacking of SrRuO₃ (SRO, 3 unit cells (u.c.))/BaTiO₃ (BTO, 3.5 u.c.)/SrRuO₃ (SRO, 3 u.c.) films grown on SrTiO₃ (STO) substrate along the [001] direction.

combination of surface X-ray scattering and COBRA. We systematically measured the crystal truncation rods (CTRs) of the SRO/BTO/SRO heterostructures in a three-dimensional reciprocal space and analyzed their electron density maps using COBRA. We visualized the atomic arrangement of the heterostructures, specifically the (200) plane and (001) plane. Additionally, we plotted the electron density along the z direction at the (0 0), (0.5 0.5), and (0 0.5) positions for the A-site ion, B-site ion, and oxygen, respectively. Based on the calculated electron

density maps, we determined the individual lattice parameters of three layers in the heterostructures and obtained a relation between the stability of ferroelectric polarization and the critical thickness.

2. Experimental methods

The SRO/BTO/SRO heterostructures were epitaxially grown on TiO₂-terminated SrTiO₃ (STO)(001) substrates using the pulsed laser deposition technique. SRO and BTO ceramic targets were ablated with a KrF excimer laser (248 nm, COMPex Pro, Coherent). The total thicknesses of the heterostructures were 10–15 u.c. for COBRA. The resolution of COBRA is a sub-Angstrom level, determined by the lattice parameter (d) and the maximum diffraction vector (L), e.g., 0.15 Å for $L = 4.3$ and $d = 3.905$ Å [19,20]. Detailed growth conditions are described elsewhere [14]. Surface X-ray scattering measurements were carried out at Sector 12-ID-D at Advanced Photon Source, Argonne National Laboratory and at Sector 5A at Pohang Accelerator Laboratory. The two-dimensional images of the CTRs were measured using an area detector (Dectris PILATUS 100K) under an X-ray photon energy of 23.5 keV or 16 keV. All specular and off-specular CTRs were analyzed using COBRA.

3. Results and discussions

Fig. 1 shows the ferroelectric BTO film (3.5 u.c.) sandwiched by the top and bottom SRO layers (3 u.c.) grown on the STO (001) substrate. The building blocks are ABO₃ perovskite structures, which consist of AO and BO₂ layers. The crystal structure of BTO at 300 K is tetragonal with $P4/mmm$ symmetry [24]. The structures of SRO and STO are orthorhombic and cubic, respectively at 300 K. The lattice parameters of perovskite STO are $a = b = c = 3.905$ Å [25]. Depending on the strain and growth conditions, those of SRO thin films can be modulated. Note that the lattice parameters of bulk SRO are $a = 5.5670$ Å, $b = 5.5304$ Å, and $c = 7.8446$ Å [22,23]. The in-plane lattice parameters of fully strained ultrathin SRO and BTO films are also identical at 3.905 Å, confirmed by X-ray scattering measurements. Based on the

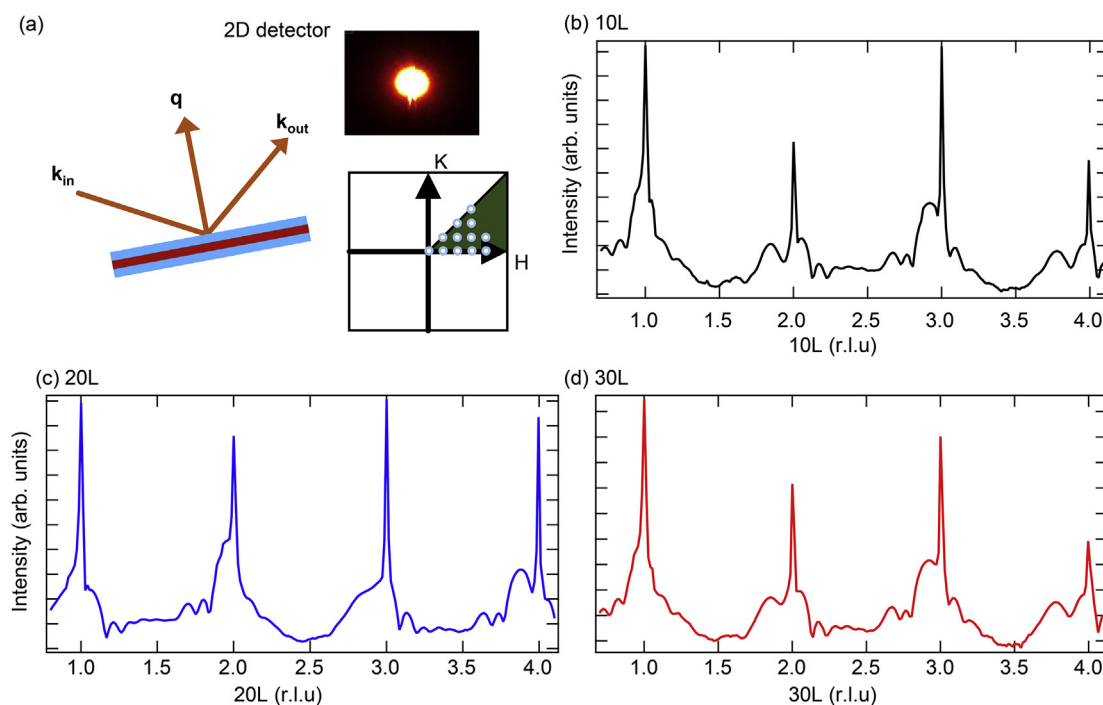


Fig. 2. Crystal truncation rod (CTR) measurements of SRO/BTO/SRO heterostructures for coherent Bragg rod analysis (COBRA). (a) Schematics of synchrotron-based X-ray scattering with area detector and measured three-dimensional reciprocal space represented by (H K L) of STO. Representative CTR data along (b) (10L), (c) (20L), and (d) (30L).

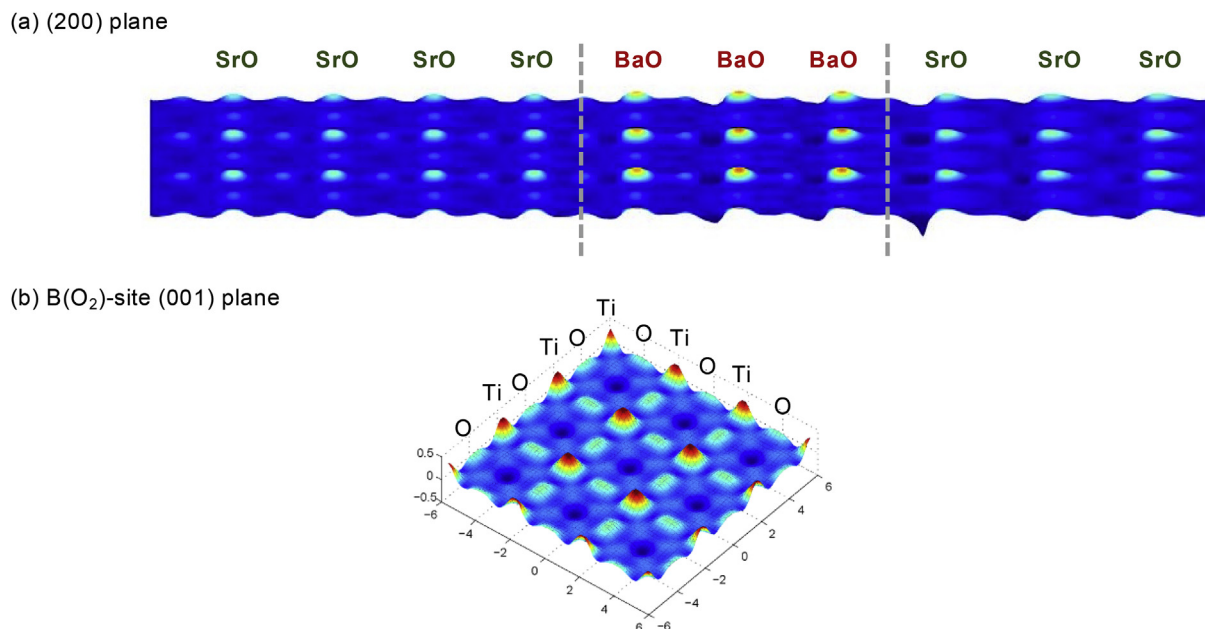


Fig. 3. Two-dimensional electron density maps obtained by COBRA. (a) (200) plane of SRO/BTO/SRO heterostructure demonstrating SrO and BaO stacking sequence. (b) (001) plane of the heterostructure, which can show TiO₂ site in the BTO layer.

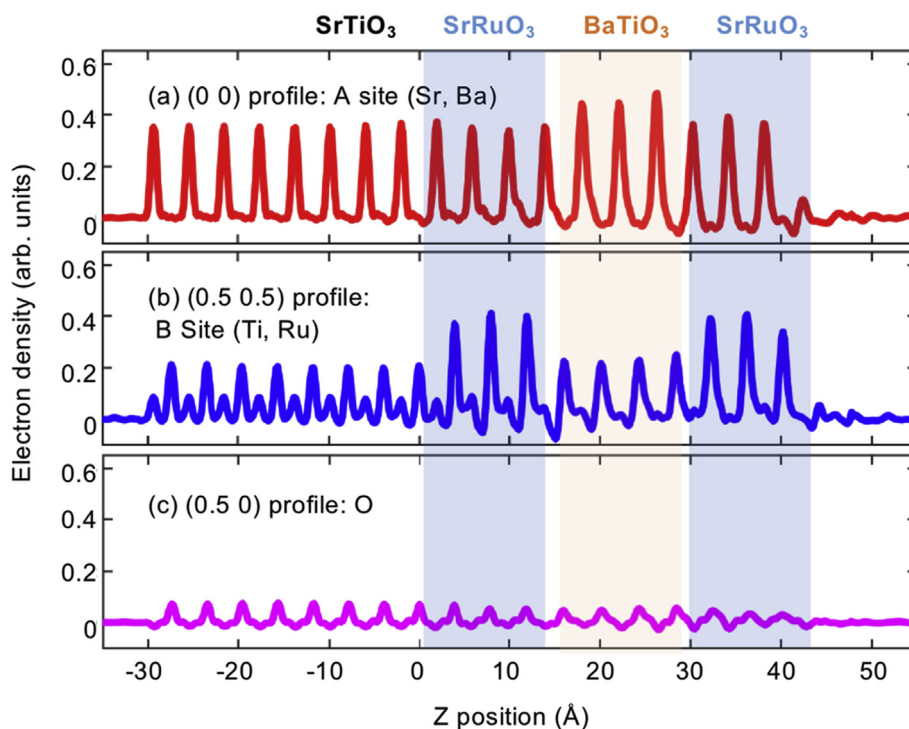


Fig. 4. COBRA-calculated electron density profiles of the heterostructure at three sites in ABO₃ perovskite structure along the z direction: (a) A-site (Sr or Ba) electron density profiles at (0, 0), (b) B-site (Ti or Ru) electron density profiles at (0.5, 0.5), and (c) O-site electron density profiles at (0.5, 0) along the [001] direction.

previous study, we manipulated the oxygen partial pressure during the BTO growth to achieve a uniform SrO–TiO₂ termination rather than a BaO–RuO₂ termination at the SRO/BTO interface owing to the thermodynamic stability of BTO [26]. We fabricated the SRO/BTO/SRO heterostructure as a model system for COBRA via the termination engineering, i.e., the atomic-level control of the stacking layer at the 0.5 u.c level.

We performed synchrotron-based surface X-ray scattering to investigate the three-dimensional crystal structure of our system, as shown in Fig. 2. Fig. 2(a) displays the schematics of the X-ray scattering

measurements carried out using a two-dimensional area detector. The scattered X-ray generates a diffraction pattern similar to a delta function from infinite periodic layers like STO single-crystal substrates. These normal Bragg peaks of STO have very strong intensities and they are easily detected via lab-source-based X-ray diffraction. However, the diffracted patterns obtained from ultrathin films are generally quite broad and have weak intensities because of finite periodicity. Additionally, they are constructed along the normal lines in the reciprocal space of the surface of the thin film. The distributions of the diffraction intensities along these lines are referred to as CTRs.

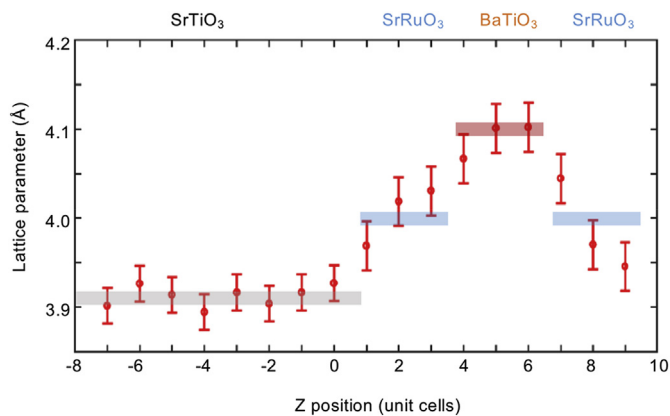


Fig. 5. Out-of-plane lattice parameters of STO, bottom SRO, BTO, and top SRO layers.

The measured representative CTR data along (10L), (20L), and (30L) of the SRO/BTO/SRO heterostructures are presented in Fig. 2(b), 2(c), and 2(d), respectively. The measured CTR data have sharp Bragg peaks at each integer originating from the STO substrate and weak but clearly noticeable patterns from ultrathin films. To reconstruct the three-dimensional atomic-level crystal structure using COBRA, we measured the complete data set with the consideration of symmetry equivalency and resolution, e.g., (00L), (10L), (11L), (20L), (21L), (22L), (30L), (31L), (32L), (33L), (40L), (41L), and (42L). The index of plane (HKL) represents the STO cubic notation.

Our method efficiently finds the appropriate electron densities of the system and the complex structure factors of our unknown structure [15–21]. The complex structure factors are calculated from the measured CTR data using the Fourier transformation and directly connected to the three-dimensional electron densities of the system. Complex structure factor \mathcal{F} is described as

$$\mathcal{F}(\vec{q}) = \int_V \rho(\vec{r}) \cdot e^{i\vec{q} \cdot \vec{r}} d^3r \quad (1)$$

where \vec{q} is the position vector in the reciprocal space, \vec{r} is the position vector in the real space, ρ is the electron density and the integral is over the volume of the sample. Firstly, \mathcal{F} is calculated for the initial model system consisting of the BTO film, top/bottom SRO layers, and STO substrates. The complex structure factor given by Eq. (1) is the linear combination of the contribution of the reference and the unknown structure related to the films, as expressed in Eq. (2).

$$\mathcal{F}_{total} = \mathcal{F}_{ref} + \mathcal{F}_{unknown} \quad (2)$$

$$\rho(\vec{r}) = \int \mathcal{F}(\vec{q}) e^{-i\vec{q} \cdot \vec{r}} d^3q \quad (3)$$

Note that the reference structure factor, \mathcal{F}_{ref} , and the unknown structure factor, $\mathcal{F}_{unknown}$, provide sharp Bragg peaks and extremely weak signals in the CTRs, as shown in Fig. 2. Second, we compare the calculated and experimental intensities. The electron density of the real space can be calculated based on \mathcal{F} using the inverse Fourier transformation given by Eq. (3). If acceptable, the result becomes the updated reference structure. Here, $\mathcal{F}_{unknown}$ can be spatially distinguished from the \mathcal{F}_{ref} based on a simple assumption, referred to as the COBRA ansatz. The ansatz states that $\mathcal{F}_{unknown}$ changes more gradually along the rod compared to \mathcal{F}_{ref} . Therefore, the difference between the updated reference and calculated electron density converges rapidly within a small number of iterations.

As shown in Fig. 3, the COBRA-based two-dimensional electron density of the planes clearly demonstrates that there are exactly three BaO layers in the heterostructure. The (200) plane in Fig. 3(a) shows the atomic-level stacking sequence, e.g., the bottom SrO, BaO, and top SrO layers. In the electron density map, the intensity (or integrated

electron density) at a specific position is correlated to the total number of electrons in the atom. Then, it is quite reasonable that the intensity at the Ba site (atomic number: 56) is higher than that at the Sr site (atomic number: 38), as shown in Fig. 3(a). The intensity at the O site (atomic number: 8) is considerably weaker compared to the other sites. Furthermore, the COBRA-based electron density map contains the three-dimensional crystal structure. Hence, we can obtain the in-plane structure, as shown in Fig. 3(b). There is a (001) plane through the Ti and O atoms close to the BTO film region.

To get further insight on the detailed interface structure, we plotted one-dimensional electron density profiles along the z-direction at three different positions in the ABO₃ perovskite structure. The profiles at (0 0), (0.5 0.5), and (0.5 0) are shown in Fig. 4 (a), (b), and (c), respectively. As mentioned earlier, three Ba layers were sandwiched by Sr layers because of the higher intensity of Ba compared to Sr. As shown in Fig. 4(b), the numbers of Ti and Ru bottom (top) layers in the SRO/BTO/SRO heterostructures were four and three (three), respectively. Note that the atomic numbers of Ru and Ti are 44 and 22, respectively. Specifically, the interface structures close to the bottom and top SRO electrodes exhibited the following stacking sequences: (bottom) RuO₂–SrO–TiO₂–1st BaO and (top) 3rd BaO–TiO₂–SrO–RuO₂. We used the COBRA to confirm that the thickness of BTO film was 3.5 u.c. and the interface structure of the heterostructure was symmetric at the atomic level.

Moreover, the electron density profiles calculated by utilizing COBRA provided the lattice parameters of each SRO and BTO layer, as shown in Fig. 5. The atomic positions along the z direction were extracted by fitting one Gaussian to each peak in the electron density profiles shown in Fig. 4. The lattice parameters were determined based on the spacing between the AO (or BO₂) layer and the next nearest AO (or BO₂) layer. Even though our initial reference model allowed for the modulation of the atomic positions of 7 u.c. STO substrate, the lattice parameter of STO was quite similar to that of bulk STO, i.e., 3.905 Å. Owing to strain and coherent growth, the in-plane lattice of the BTO layer was clamped with that of SRO (or STO) and the out-of-plane lattice parameters of the BTO layers were approximately 4.08 Å. It is interesting to note that the out-of-plane lattice parameters of the top and bottom SRO electrodes were significantly altered by the BTO layers. The direction of polarization and octahedral rotation should be investigated further.

4. Conclusion

In summary, we determined the atomic-level structural properties of the SrRuO₃/BaTiO₃/SrRuO₃ (SRO/BTO/SRO) heterostructures using Coherent Bragg Rod Analysis (COBRA) method. COBRA based on crystal truncation rod scans could visualize the three-dimensional atomic arrangement of the heterostructures. We confirmed that the BTO layer was 3.5 unit cells and the SRO/BTO/SRO heterostructures exhibited a symmetric interface, which can enhance ferroelectric stability. Furthermore, we quantitatively defined the positions of atoms and determined the individual lattice parameters of the three layers in the heterostructures. COBRA exhibits high potential for investigating the detailed structural and physical properties of ultrathin films and oxide heterostructures.

Declaration of competing interest

The authors declare that they have no known competing financial interests or personal relationships that could have appeared to influence the work reported in this paper.

Acknowledgments

K.J.L. and Y.J.S. contributed equally to this work. The work was supported by the Chung-Ang University Graduate Research Scholarship

in 2018 (awarded to K.J.L.). This research also was supported by the Research Center Program of the IBS in Korea (grant no. IBS-R009-D1, awarded to Y.J.S. and T.W.N.). Use of the Advanced Photon Source was supported by the U.S. Department of Energy, Office of Science, Office of Basic Energy Sciences, under Contract No. DE-AC02-06CH11357.

References

- [1] H.Y. Hwang, Y. Iwasa, M. Kawasaki, B. Keimer, N. Nagaosa, Y. Yokura, Emergent phenomena at oxides interfaces, *Nat. Mater.* 11 (2012) 103.
- [2] J. Mannhart, D.G. Schlom, Oxides interfaces—an opportunity for electronics, *Science* 327 (2010) 1607.
- [3] A.K. Yadav, C.T. Nelson, S.L. Hsu, Z. Hong, J.D. Clarkson, C.M. Schelpüetz, A.R. Damodaran, P. Shafer, E. Arenholz, L.R. Dedon, D. Chen, a. Vishwanath, A.M. Minor, L.Q. Chen, J.F. Scott, L.W. Martin, R. Ramesh, Observation of polar vortices in oxide superlattices, *Nature* 530 (2016) 198.
- [4] A. Ohtomo, H.Y. Hwang, A high-mobility electron gas at the $\text{LaAlO}_3/\text{SrTiO}_3$ heterointerface, *Nature* 427 (2004) 423.
- [5] J. Heber, Material science: enter the oxides, *Nature* 459 (2009) 28.
- [6] J. Chakhalian, A.J. Millis, J. Rondinelli, Wither the oxide interface, *Nat. Mater.* 11 (2012) 92–94.
- [7] P. Zubko, S. Gariglio, M. Gavay, P. Ghosez, J.-M. Triscone, Interface physics in complex oxide heterostructures, *Annu. Rev. Condens. Matter Phys.* 2 (2011) 141–165.
- [8] M. Huijben, A. Brinkman, G. Koster, G. Rijnders, H. Hilgenkamp, D.H.A. Blank, *Adv. Mater.* 21 (2009) 1665.
- [9] N. Reyren, S. Thiel, A.D. Caviglia, L. Fitting Kourkoutis, G. Hammerl, C. Richter, C.W. Schneider, T. Kopp, A.-S. Rüetschi, D. Jaccard, M. Gabay, D.A. Muller, J.-M. Triscone, J. Mannhart, Superconducting interfaces between insulating oxides, *Science* 317 (2007) 1196–1199.
- [10] D. Xiao, W. Zhu, Y. Ran, N. Nagaosa, S. Okamoto, Interface engineering of quantum Hall effects in digital transition metal oxide heterostructures, *Nat. Commun.* 2 (2011) 596–598.
- [11] M. Stengel, D. Vanderbilt, N.A. Spaldin, Enhancement of ferroelectricity at metal-oxide interfaces, *Nat. Mater.* 8 (2009) 392.
- [12] J. Junquera, P. Ghosez, Critical thickness for ferroelectricity in perovskite ultrathin films, *Nature* 422 (2003) 506.
- [13] G. Gerra, A.K. Tagantsev, N. Setter, K. Parlinski, Ionic polarizability of conductive metal oxides and critical thickness for ferroelectricity in BaTiO_3 , *Phys. Rev. Lett.* 96 (2006) 107603.
- [14] Y.J. Shin, Y. Kim, S.-J. Kang, H.-H. Nahm, P. Murugavel, J.R. Kim, M.R. Cho, L. Wang, S.M. Yang, J.-G. Yoon, J.-S. Chung, M. Kim, H. Zhou, S.H. Chang, T.W. Noh, Interface control of ferroelectricity in an $\text{SrRuO}_3/\text{BaTiO}_3/\text{SrRuO}_3$ capacitor and its critical thickness, *Adv. Mater.* 29 (2017) 1602795.
- [15] Y. Yacoby, H. Zhou, R. Pindak, I. Božovic, Atomic-layer synthesis and imaging uncover broken inversion symmetry in $\text{La}_{2-x}\text{Sr}_x\text{CuO}_4$ films, *Phys. Rev. B* 87 (2013) 014108.
- [16] D.D. Fong, C. Cionca, Y. Yacoby, G.B. Stephenson, J.A. Eastman, P.H. Fuoss, S.K. Streiffer, Carol Thompson, R. Clarke, R. Pindak, E.A. Stern, Direct structural determination in ultrathin ferroelectric films by analysis of synchrotron X-ray scattering measurements, *Phys. Rev. B* 71 (2005) 144112.
- [17] H. Zhou, Y. Yacoby, V.Y. Butko, G. Logvenov, I. Božovic, R. Pindak, Anomalous of expansion of the copper-apical-oxygen distance in superconducting cuprate bilayers, *Proc. Natl. Acad. Sci. U.S.A.* 107 (2010) 8103.
- [18] C.N. Cinoca, D.A. Walko, Y. Yacoby, C. Dorin, J.M. Millunchick, R. Clarke, Interfacial structure, bonding and composition of InAs and GaSb thin films determined using coherent Bragg rod analysis, *Phys. Rev. B* 75 (2007) 115306.
- [19] Y. Yacoby, R. Pindak, R. MacHarrie, L. Pfeiffer, L. Berman, R. Clarke, Direct structure determination of systems with two-dimensional periodicity, *J. Phys. Condens. Matter* 12 (2001) 3929.
- [20] Y. Yuan, Y. Lu, G. Stone, K. Wang, C.M. Brooks, D.G. Schlom, S.B. Sinnott, H. Zhou, V. Gopalan, Three-dimensional atomic scale electron density reconstruction of octahedral tilt epitaxy in functional perovskites, *Nat. Commun.* 9 (2018) 5220.
- [21] C.W. Jones, P.D. Battle, P. Lightfoot, T.A. Harrison, The structure of SrRuO_3 by time-of-flight neutron powder diffraction, *Acta Crystallogr. Sect. C Cryst. Struct. Commun.* 45 (1989) 365.
- [22] S.H. Chang, Y.J. Chang, S.Y. Jang, D.W. Jeong, C.U. Jung, Y.-J. Kim, J.-S. Chung, T.W. Noh, *Phys. Rev. B* 84 (2011) 104101.
- [23] M.C. Wittels, F.A. Sherrill, Fast neutron effects in tetragonal barium titanate, *J. Appl. Phys.* 28 (1957) 606.
- [24] S.A. Howard, J.K. Yau, H.U. Anderson, Structural characteristics of $\text{Sr}_{1-x}\text{La}_x\text{TiO}_{3+d}$ as a function of oxygen partial pressure at 1400°C , *J. Appl. Phys.* 65 (1989) 1492.
- [25] Y.J. Shin, L. Wang, Y. Kim, H.-H. Nahm, D. Lee, J.R. Kim, S.M. Yang, J.-G. Yoon, J.-S. Chung, M. Kim, S.H. Chang, T.W. Noh, *ACS Appl. Mater. Interfaces* 9 (2017) 27305.